https://doi.org/10.1038/s44306-025-00083-2

Revisiting altermagnetism in RuO_2: a study of laser-pulse induced charge dynamics by time-domain terahertz spectroscopy

David T. Plouff[1] ✉, Laura Scheuer[1], Shreya Shrestha[1], Weipeng Wu[1], Nawsher J. Parvez[1], Subhash Bhatt[1], Xinhao Wang[1], Lars Gundlach[1,2] ✉, M. Benjamin Jungfleisch[1] ✉ & John Q. Xiao[1] ✉

RuO_2 is one of the most studied altermagnetic candidate materials. However, it has recently been scrutinized as evidence emerged for its lack of any magnetic order. In this work, we study bilayers of epitaxial RuO_2 and ferromagnetic permalloy ($Fe_{19}Ni_{81}$) by time-domain terahertz spectroscopy, probing for three mechanisms of laser-induced charge dynamics: the inverse spin Hall effect (ISHE), electrical anisotropic conductivity (EAC), and inverse altermagnetic spin-splitting effect (IASSE). We examine four orientations of RuO_2: (001), (100), (110), and (101). Our results are consistent with charge dynamics induced by only the ISHE and EAC and do not indicate the presence of IASSE for either as-deposited or field-annealed samples, casting further doubt on the existence of altermagnetism in RuO_2. In addition, we find that the combination of ISHE and EAC in the (101) oriented sample produces THz emission that is tunable between linear and elliptical polarization by modulation of the external magnetic field.

Altermagnetism is a newly identified magnetic phase characterized by collinear antiferromagnetism coexisting simultaneously with anisotropic spin-splitting in the band structure, owing to the two spin-sublattices being connected by a real space rotation symmetry[1]. Altermagnet materials are poised to have a significant impact in the field of spintronics, as there is already a significant effort underway to replace ferromagnet-based technologies with antiferromagnets, which host faster magnetization dynamics and lack of stray field[2]. While the spin-degenerate band structure of antiferromagnets makes their Néel state difficult to detect, the spin-splitting in altermagnets is predicted to produce novel spin-transport phenomena that are Néel vector dependent, thus overcoming the challenges faced by traditional collinear antiferromagnets. Since the prediction of altermagnetism[3–6], the spintronics field has invested significant research effort in finding altermagnetic candidate materials, with none more popular than rutile RuO_2. Although it had long been considered a paramagnet[7], in 2017, a report of neutron scattering provided the first indication suggesting the existence of collinear antiferromagnetism along the *c*-axis with a small moment of 0.05 μ_B per Ru atom[8]. While many subsequent studies reported positive indications for altermagnetism in RuO_2[9–17], recent probes for the ordered antiferromagnetism by neutron scattering, muon spin rotation, and spin and angle-resolved photoelectron spectroscopy have suggested no ordered antiferromagnetism or altermagnetic band structure[18–20].

Here, we investigate epitaxial RuO_2 in bilayer with ferromagnetic (FM) permalloy ($Fe_{19}Ni_{81}$) by time-domain terahertz (THz) spectroscopy (TDTS), probing for three possible mechanisms of laser-pulse (LP) induced charge dynamics: the relativistic inverse spin Hall effect (ISHE), the non-relativistic inverse altermagnetic spin-splitting effect (IASSE), and the non-relativistic and non-magnetic electrical anisotropic conductivity (EAC). It is well known that FM/normal-metal(NM) bilayers can be excited by a femtosecond (fs)-LP to produce an ultrafast demagnetization process accompanied by charge dynamics that produce THz radiation, called a spintronic emitter (SE)[21–24]. The common interpretation is that the ultrafast demagnetization causes a spin current ($\vec{J}_s$) to be injected from the FM into the NM, which then converts to a transverse charge current ($\vec{J}_c$) by the ISHE, following the equation $E_{THz} \propto \vec{J}_c = \theta_{SH}\vec{J}_s \times \vec{\sigma}$, where θ_{SH} is the spin Hall angle of the NM layer and $\vec{\sigma}$ is the spin-polarization. Recently, the IASSE and EAC were reported for the first time as novel non-relativistic THz emission mechanisms, both in heterostructures comprising RuO_2[15,25]. While the EAC mechanism only requires RuO_2 to be metallic and an epitaxial

[1]Department of Physics and Astronomy, University of Delaware, Newark, DE, USA. [2]Department of Chemistry and Biochemistry, University of Delaware, Newark, DE, USA. ✉e-mail: dplouff@udel.edu; larsg@udel.edu; mbj@udel.edu; jqx@udel.edu

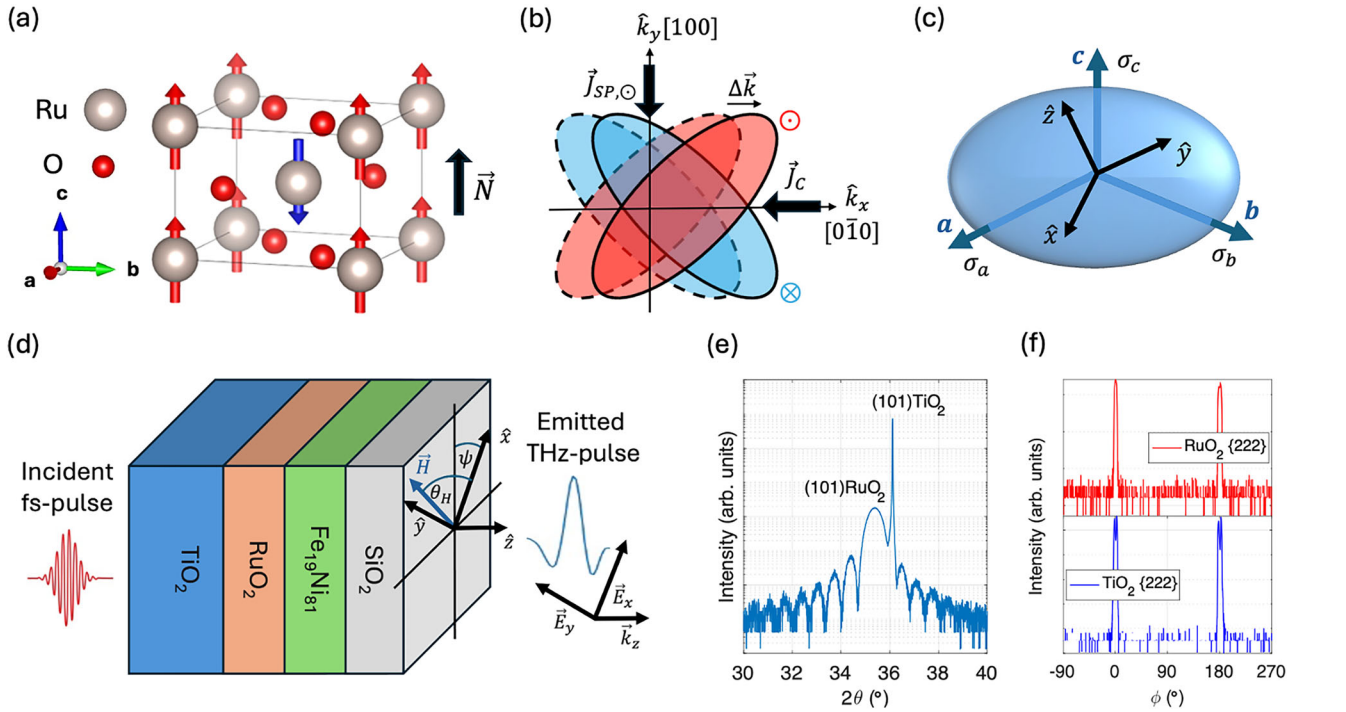

Fig. 1 | Crystal structure, anisotropic spin/charge conductivities, and diagram of experiment. a Rutile RuO_2 unit cell with proposed antiferromagnetic spins along the c-axis, **b** proposed spin-split Fermi surface of d-wave altermagnetism in RuO_2, **c** ellipsoidal conductivity tensor with the lab frame coordinates rotated relative to the crystal axes, **d** diagram of experimental setup for TDTS measurement with ψ being the angle between the laboratory frame ($\hat{x},\hat{y},\hat{z}$) and the principle crystal axis, **e** HRXRD $\theta/2\theta$ measurement of (101) oriented sample and **f** in-plane ϕ scan of the asymmetric {222} planar family in both the film (red) and substrate (blue).

anisotropic crystal, the IASSE requires ordered antiferromagnetism and an altermagnetic band structure. The tetragonal unit cell with proposed antiferromagnetic spins along the c-axis is shown in Fig. 1a (image produced using the VESTA software[26]), and the corresponding spin-split altermagnetic Fermi surface is shown in Fig. 1b. Figure 1c shows the ellipsoid conductivity tensor of RuO_2, which we reiterate does not depend on the presence of antiferromagnetism or altermagnetism. If RuO_2 is an altermagnet and not an NM, the IASSE mechanism should lead to spin-to-charge conversion that can contribute to the THz emission when the injected spin current $\vec{J}_s$ has a projection along the [100] direction and the spin-polarization $\vec{\sigma}$ has a projection along the Néel vector $\vec{N}$, as illustrated in Fig. 1b. The EAC mechanism, however, does not involve either $\vec{J}_s$ or $\vec{N}$, but only requires a charge current $\vec{J}_c$ injected along a crystal direction which has off-diagonal conductivity tensor terms. In fact, in reference[25], no FM layer is used, and so no spin current is related to their observed THz emission. The EAC mechanism is simply based on Ohm's law, $\vec{J}_c = \sigma\vec{E}$, where the conductivity tensor σ is anisotropic because of the rutile crystal structure, with $\sigma_a = \sigma_b > \sigma_c$. Orientations that contain components of both the *a* and *c*-axis lattice parameters projecting in the out-of-plane direction ($\hat{z}$) will thus show EAC-based THz emission. In our work, we use rutile TiO_2 substrates to achieve epitaxial growth of the RuO_2 layer of four common orientations in order to study the crystal direction-dependent conversion: (001), (100), (110), and (101). Given that the altermagnetic band structure is a direct consequence of the real space crystal structure, it is advantageous to use a single crystal or epitaxial thin film to properly probe the crystal direction-dependent phenomena. An example of the high-quality epitaxial nature of our films, grown by reactive magnetron sputtering, is shown in Fig. 1e, f. The high-resolution X-ray diffraction (HRXRD) $\theta/2\theta$ scan shows many Laue oscillations, and the in-plane ϕ scan shows a single in-plane phase that is matched with the substrate, as is the case for all our samples, which are reported in the supplemental information (SI) Figs. S1 and S2. THz emission from the samples is measured by TDTS. A laser-pulse incident from the substrate side pumps the spin-polarized charge current that is subsequently injected from the permalloy into the RuO_2 along the $-\hat{z}$ direction. The spin-polarization is controlled by the rotation of the applied magnetic field angle θ_H, as depicted in Fig. 1c. The *x* and *y* components of the emitted THz electric field are measured as a function of θ_H and integrated to find the root mean square value of the emitted amplitude, E_{rms}. We emphasize that we utilized substrate side laser excitation to prevent the TiO_2 substrates THz absorption and birefringence from modulating the emitted THz signal.

Results

THz emission from non-EAC orientations of RuO_2: (001), (100), and (110)

We first consider the samples with RuO_2 layer orientations that are not expected to have emission by EAC, i.e., the (001), (100), and (110) orientations, which have only the *a*- or *c*-axes in the out-of-plane direction, and thus have no off-diagonal conductivity tensor terms for a current injected along $-\hat{z}$. Polar plots of the measured E_{rms} under varied θ_H are reported in Fig. 2. For the (001) sample in Fig. 2a, the emitted THz amplitude is clearly isotropic and well described by a circle, which is consistent with spin-to-charge conversion by the ISHE only, as expected for RuO_2 being either a NM or an altermagnet. For the (100) and (110) oriented samples in Fig. 2b–d, the emitted THz amplitude is found to be slightly anisotropic, with the stronger emission occurring when the magnetization is parallel to the *c*-axis of the crystals at $\theta_H = 90°$. We argue that the in-plane EAC of those samples causes the anisotropy and not the IASSE. This matter is further discussed in the "Discussion" section.

It is important to note that, in contrast to our results, the THz emission reported in reference[15] that was attributed to the IASSE was only observed after field annealing of the samples. Additionally, their results indicated that the IASSE contribution to the emission varies strongly with thickness, with the strongest emission occurring for a 5 nm thick RuO_2 layer. In contrast, our results in Fig. 2b, d show that the emission intensity (blue data points) is

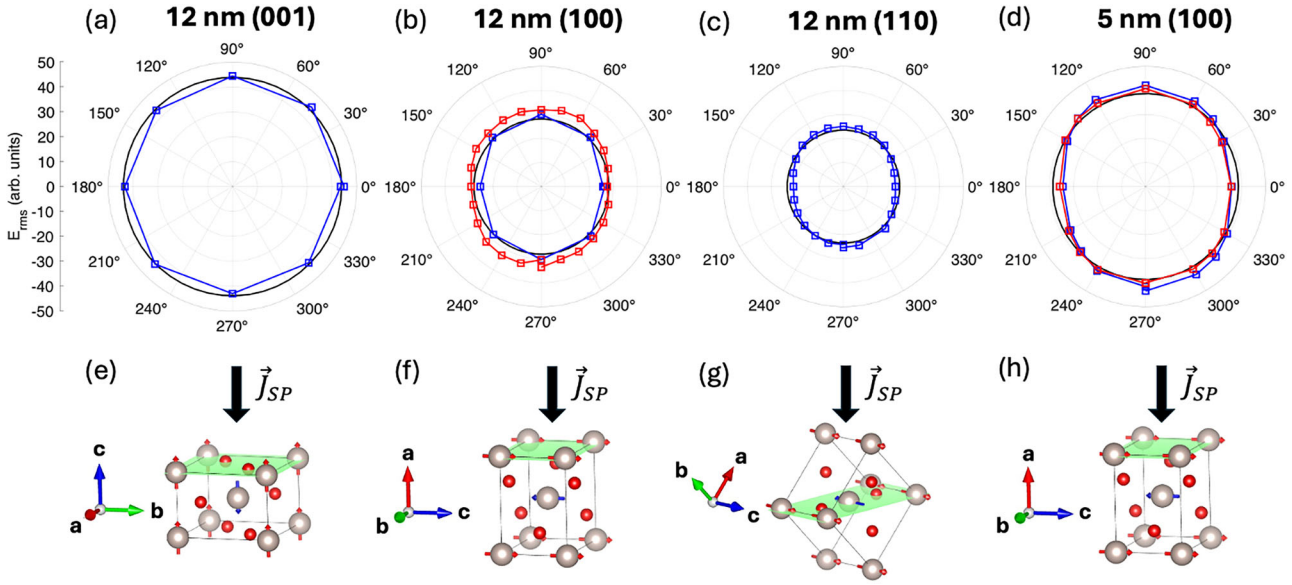

Fig. 2 | E_{rms} as a function of external field angle θ_H for samples without EAC. **a** (001), **b** (100), and **c** (110) samples with 12 nm thick RuO_2 layer, and **d** for (100) oriented sample with 5 nm thick RuO_2 layer. Blue data points are from as-deposited samples, red data points are post field annealing, and black circles are guides to the eye (with a radius equal to the as-deposited E_{rms} average). **e**–**h** show the relative orientation of the injected spin current to the crystal structure and proposed Néel vector for each sample, respectively.

essentially the same for the (100) oriented samples with 12 and 5 nm thick RuO_2 layer. In addition, the emission is unchanged after field annealing following the same protocol used in reference[15], i.e., annealing at 475 K for 2 h and subsequent cooling in an 8 kG field (red data points).

THz emission from (101) oriented RuO_2

We now consider the (101) oriented sample. It has already been demonstrated that metallic (101) oriented rutile RuO_2 and IrO_2 generate THz emission by the non-magnetic and non-relativistic EAC mechanism that is enhanced by an additional NM layer[25]. However, the effect of the EAC mechanism on a spin current that is injected from an FM layer into the (101) RuO_2 film has not yet been explored. Considering that both the IASSE and ISHE change sign when reversing the spin-polarization of the injected spin current, but the EAC does not, we expect that the EAC contribution to the THz emission can be isolated by reversing the magnetic field direction. Adding the THz emission collected at θ_H and $\theta_H + 180°$ and dividing by two (Equation (1)) results in the EAC contribution that does not depend on the field direction.

$$E_{x,y,EAC} = (E_{x,y}(\theta_H) + E_{x,y}(\theta_H + 180°))/2 \quad (1)$$

The x and y components of the total measured signal for the (101) sample at crystal angle $\psi = 0°$ (see Fig. 1c) and field angle $\theta_H = 90°$ are plotted in the time-domain in Fig. 3a, the extracted EAC component of the signal is plotted in Fig. 3b, and the total signal remaining after subtracting the EAC component is shown in Fig. 3c. In Fig. 3d–h, parametric plots of the x and y components of the emitted electric field for the signal excluding the EAC component is shown in blue, the EAC component is shown in red, and the total THz emission is shown in yellow. It can clearly be seen that the combination of the two emission mechanisms (ISHE and EAC) can result in elliptically polarized light depending on the direction of the external magnetic field (e.g., yellow for $\theta_H = 90°$).

Figure 4 shows a polar plot of the E_{rms} of the total emitted THz signal in yellow and the signal excluding the EAC component in blue. Figure 4a, b illustrate that the EAC component follows the rotation of the crystal by the angle ψ (red arrow), as expected. The signal excluding EAC (blue) shows the same small anisotropy that was observed for the (100) and (110) samples (Fig. 2b–d) that will be discussed below.

Discussion

We postulate that the small anisotropy of the THz emission observed in the (100), (110), and (101) oriented samples is due to in-plane EAC of RuO_2, which modulates the in-plane charge currents that result from the ISHE. To illustrate the out-of-plane EAC mechanism of THz emission, and the in-plane EAC effect on THz emission from ISHE, the 2D projections of the conductivity tensor are shown in Fig. 5. Panels (a–e) show the x-z planes of each (hkl) orientation, (f–j) show the y-z plane, and (k–o) shows the x-y plane. Since the (100), (110), and (101) oriented films contain both the a and c-axis of the lattice in their plane, the in-plane projection of the conductivity tensor is elliptical. When the external field is rotated, the in-plane charge current produced by the ISHE experiences different conductivities depending on the crystal directions; the amplitude of the current decays faster in the less conductive σ_c direction. While we do not measure the direction-dependent in-plane conductivity of our samples, it is known that the rutile crystal of RuO_2 shows anisotropic conductance. Since we observe EAC-induced THz emission from our (101) RuO_2 sample, EAC is expected to exist in RuO_2 samples with other orientations.

To exclude that the small anisotropy in the THz emission amplitude is caused by magnetic anisotropy in the FM layer, we measured in-plane magnetization hysteresis loops of each sample along both flat edge directions by vibrating sample magnetometry (VSM) and report the results in the SI (Figs. S3–S5). We observe an easy and hard axis in each sample that showed anisotropy in the THz emission amplitude, however the hard axis magnetic anisotropy field H_a is less than 1 kG for any given sample, so it is reasonable to expect that all samples were saturated by the external applied field with a field strenth of 1.4 kG. The high symmetry (001) sample had an easy-plane magnetic anisotropy.

If RuO_2 was an altermagnet, we would expect to observe THz emission from the IASSE in the (100) and (101) films. The linear polarization of the IASSE-induced emission should follow the rotation of the external magnetic field that aligns $\vec{\sigma}$ relative to the Néel vector. However, our measurements can be explained by a combination of ISHE, out-of-plane, and in-plane EAC. As discussed above, the small anisotropy of THz emission amplitude can be explained by in-plane EAC, if it were induced by IASSE, it should be absent for the (110) sample, for which the IASSE is forbidden. In addition, the THz emission anisotropy is essentially the same for both as-prepared and field-annealed (100)

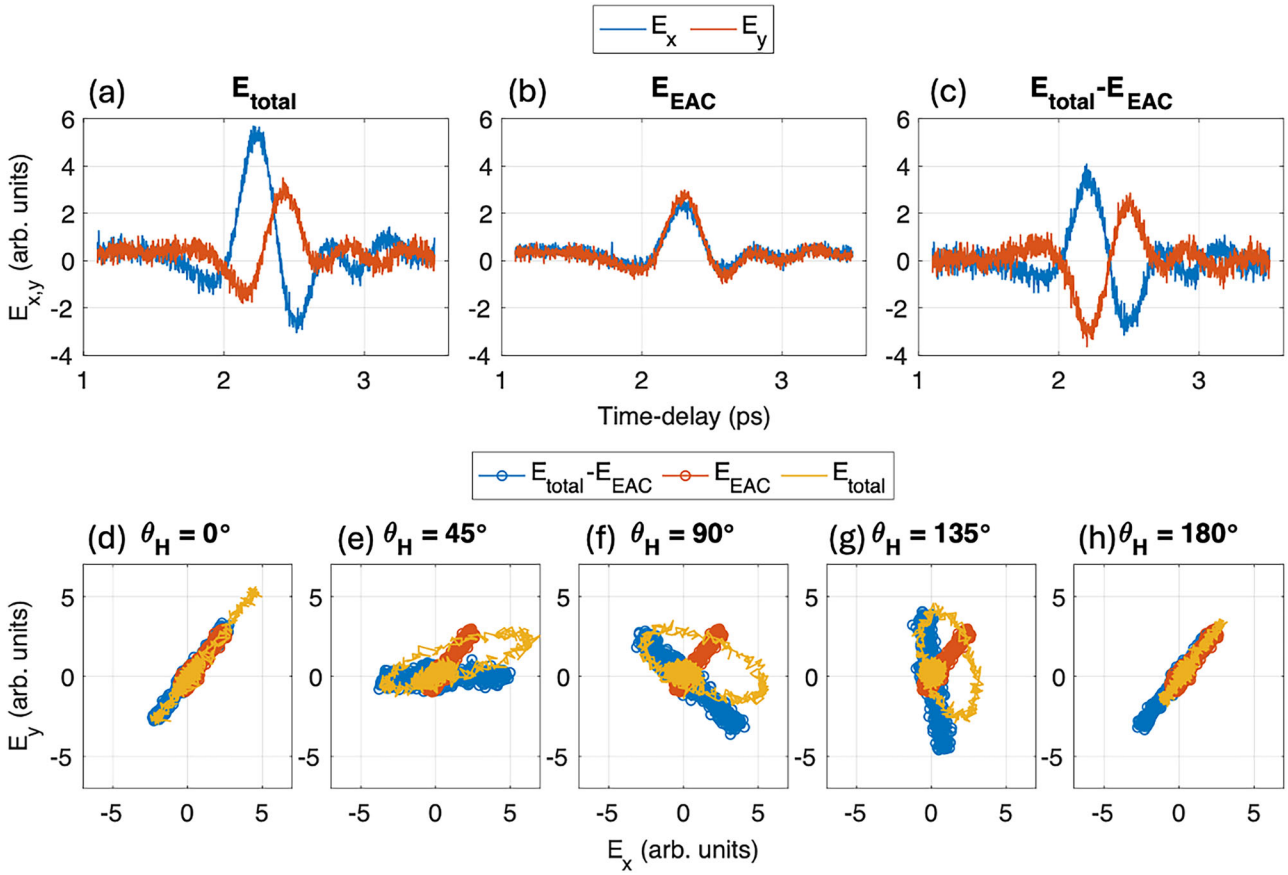

Fig. 3 | Separation of spin and EAC component signals and demonstration of modulating the emitted THz polarization. Time-domain traces of the emitted THz wave electric field components of (101) oriented sample with 12 nm thick RuO_2 layer at $\psi = 0°$ and $\theta_H = 90°$ **a** total electric field, **b** EAC component, and **c** total electric field with EAC component subtracted. **d**–**h** Parametric plots of E_x vs E_y for field angles between $\theta_H = 0°$ and 180°, with total signal (yellow), EAC component (red), and total signal minus EAC component (blue).

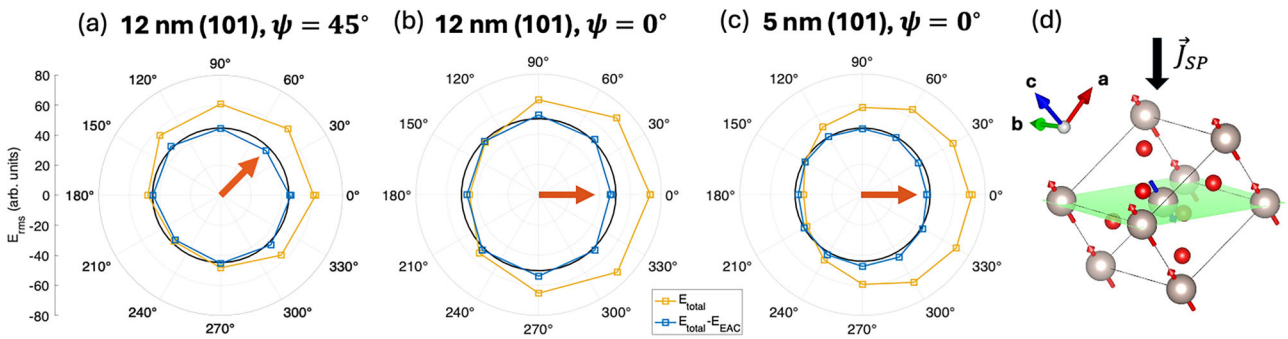

Fig. 4 | E_{rms} as a function of external field angle θ_H for the (101) samples with EAC. **a** The 12 nm sample at $\psi = 45°$, and **b** at $\psi = 0°$. **c** The 5 nm thick RuO_2 sample at $\psi = 0°$. The red arrows indicate the direction of the EAC emission, yellow data points represent the total signal, and blue data points represent the total signal with the EAC component subtracted. **d** shows the relative orientation of the injected spin current to the crystal structure and the proposed Néel vector.

samples (Fig. 2b, d). However, one would expect field annealing above the Néel temperature of ≈400 K would align the antiferromagnetic domains and enhance the IASSE signal. These results clearly demonstrate the absence of the IASSE in our RuO_2 films. Our findings align with recent observations from neutron and muon spin rotation experiments[18,19]. Notably, all our samples were epitaxially grown on single crystal TiO_2 substrates, whereas in reference[15], the use of cubic MgO and YSZ substrates are known to result in multiple in-plane crystal phases of RuO_2, which could be related to the reported anisotropy of THz emission amplitude. Our results prompt a reexamination of theoretical models and suggest further research to determine whether defects and stoichiometry of RuO_2 films may account for the varying experimental outcomes regarding the presence or absence of IASSE in RuO_2.

We emphasize that the results from the (101) oriented sample give rise to a novel method for producing elliptical polarized THz light due to the superposition of THz radiation from two sources (ISHE and EAC). The tunability of the polarization direction of THz from ISHE by an external magnetic field gives control over the ellipticity and chirality of the resulting field. In addition, unlike the ISHE, which predominantly occurs at interfaces within the spin diffusion length of RuO_2, the emission from the EAC effect is a bulk phenomenon. Thus, by adjusting the RuO_2 layer thickness, it is possible to control the relative phase between the two emitters, offering

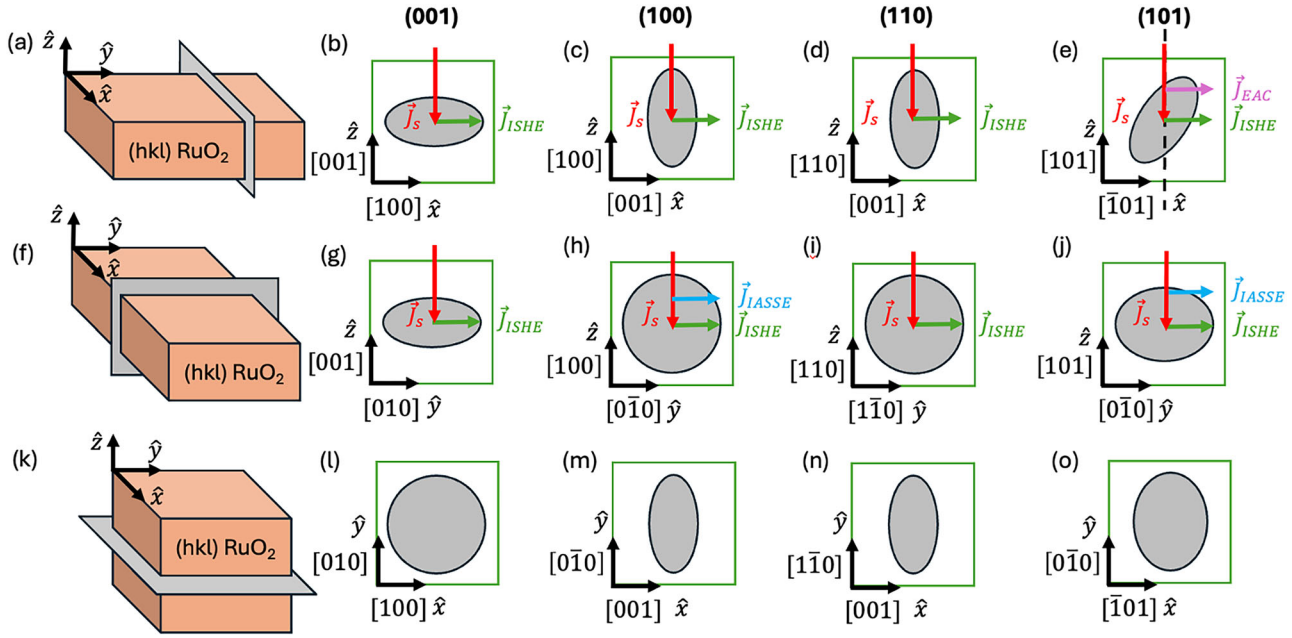

Fig. 5 | 2D projection of the ellipsoidal conductivity tensor for each sample orientation. a, **f**, and **k** illustrate the plane of the sample examined for each row of projections. **b**–**e** are the *x*-*z* plane, **g**–**j** the *y*-*z* plane, and **l**–**o** the *x*-*y* plane. In panels containing the $\hat{z}$ direction, the pumped spin current $\vec{J}_{sp}$ is polarized into the plane, and the three possible THz emission mechanisms (ISHE, IASSE, and EAC) are included with their appropriate crystal direction dependencies.

flexible options for pulse shaping. Although recently, a hybrid THz emitter consisting of a photo-conductive antenna (PCA) and SE have been combined to produce elliptical polarized THz[27], the current method is more straightforward and can be easily implemented without the need for patterning a PCA structure. Other methods to achieve polarization and pulse shape control of THz waves require modulation and filtering, which limits other wave properties such as bandwidth[28–30]. The EAC and ISHE both produce essentially the same bandwidth of THz frequencies, whereas the combination of PCA and SE hybrid emitters relies on the PCA component, which is limited to approximately 3 THz bandwidth. Our elliptical emitter can be optimized by using an EAC material with higher spin-orbit coupling (SOC) or otherwise higher β parameter as described by Zhang et al. in ref. 25, such as using IrO_2 instead of RuO_2. Addition of a high-SOC NM layer in between the EAC and FM layers could also improve emission strength by enhancing the ISHE signal from the FM and also possibly pumping more charge current into the EAC layer.

We have studied the laser-pulse induced charge dynamics in high-quality epitaxial RuO_2 and permalloy bilayers by TDTS. Our results reveal no evidence of the IASSE signature of altermagnetism in either the (100) or (101) orientations for which it is expected, including after field annealing of the (100) samples. However, we observed the non-magnetic and non-relativistic EAC emission in the (101) oriented sample. We also observe for the first time an angle-dependent THz amplitude in the (100), (110), and (101) oriented samples that we assign to in-plane modulation of the ISHE converted charge current by EAC. We demonstrated that the combination of ISHE and EAC THz emission mechanisms in the (101) oriented sample can generate elliptically polarized THz emission with chirality modulated by the applied magnetic field. Our findings imply that RuO_2 is a normal metal and not an altermagnet, and establish a novel, easily implemented approach for generating tunable, elliptically polarized THz light using an external field.

Methods

Sample fabrication

RuO_2 films were deposited on double side polished TiO_2 substrates by reactive magnetron sputtering in a vacuum chamber with base pressure of 5×10^{-8} Torr. Substrates were heated to 600 °C and baked for 10 min prior to deposition. The Ru target was sputtered with 200 W RF power in an atmosphere of 5:1 Ar/O_2 gas mixture with a total pressure of 15 mTorr. Subsequent layers of 8 nm thick permalloy ($Fe_{19}Ni_{81}$) and 10 nm thick SiO_2 capping layer were deposited in-situ after cooling substrates to room temperature, using 5 mTorr total pressure of Ar and RF bias of 100 and 200 W, respectively. The permalloy target was pre-sputtered for 10 min to clean any oxide from the target surface.

High-resolution X-ray diffraction

X-ray diffraction patterns were measured using a Rigaku Smartlab diffractometer with a Ge (220) double bounce monochromator.

Vibrating sample magnetometry

A Quantum-Design VersaLab vibrating sample magnetometer was used to measure room temperature hysteresis loops with an in-plane magnetic field. Field annealing of the (100) samples was performed in the VSM using an oven sample holder.

Time-domain terahertz spectroscopy

Samples were illuminated from the substrate side (to eliminate the substrate birefringence effect on the polarization of the emitted THz wave) with a laser pulse of approximately 40 fs in pulse duration and a center wavelength of 800 nm at 10 kHz. The beam diameter was approximately 1 mm, and the laser fluence was 2.23 mJ/cm^2. The emitted THz wave was measured using electro-optic sampling with a 1 mm thick (110)-ZnTe crystal. The sample was placed in a constant field of 1.4 kG provided by a pair of permanent magnets, which were rotated relative to the sample. A pair of THz polarizers was used to extract the total electric field of the THz radiation.

Data availability

All data is available upon request from dplouff@udel.edu.

Received: 13 December 2024; Accepted: 3 April 2025;
Published online: 13 May 2025

References

1. Šmejkal, L., Sinova, J. & Jungwirth, T. Emerging research landscape of altermagnetism. *Phys. Rev. X* **12**, 040501 (2022).

2. Jungfleisch, M. B., Zhang, W. & Hoffmann, A. Perspectives of antiferromagnetic spintronics. *Phys. Lett. A* **382**, 865–871 (2018).
3. Hayami, S., Yanagi, Y. & Kusunose, H. Momentum-dependent spin splitting by collinear antiferromagnetic ordering. *J. Phys. Soc. Jpn.* **88**, 123702 (2019).
4. Yuan, L.-D., Wang, Z., Luo, J.-W., Rashba, E. I. & Zunger, A. Giant momentum-dependent spin splitting in centrosymmetric low-z antiferromagnets. *Phys. Rev. B* **102**, 014422 (2020).
5. Šmejkal, L., González-Hernández, R., Jungwirth, T. & Sinova, J. Crystal time-reversal symmetry breaking and spontaneous Hall effect in collinear antiferromagnets. *Sci. Adv.* **6**, eaaz8809 (2020).
6. Mazin, I. I., Koepernik, K., Johannes, M. D., González-Hernández, R. & Šmejkal, L. Prediction of unconventional magnetism in doped fesb2. *Proc. Natl Acad. Sci. USA* **118**, e2108924118 (2021).
7. Ryden, W. & Lawson, A. Magnetic susceptibility of Iro2 and Ruo2. *J. Chem. Phys.* **52**, 6058–6061 (1970).
8. Berlijn, T. et al. Itinerant antiferromagnetism in Ruo 2. *Phys. Rev. Lett.* **118**, 077201 (2017).
9. Bai, H. et al. Observation of spin splitting torque in a collinear antiferromagnet Ruo 2. *Phys. Rev. Lett.* **128**, 197202 (2022).
10. Bose, A. et al. Tilted spin current generated by the collinear antiferromagnet ruthenium dioxide. *Nat. Electron.* **5**, 267–274 (2022).
11. Feng, Z. et al. An anomalous Hall effect in altermagnetic ruthenium dioxide. *Nat. Electron.* **5**, 735–743 (2022).
12. Guo, Y. et al. Direct and inverse spin splitting effects in altermagnetic Ruo2. *Adv. Sci.* **11**, 2400967 (2024).
13. Karube, S. et al. Observation of spin-splitter torque in collinear antiferromagnetic Ruo 2. *Phys. Rev. Lett.* **129**, 137201 (2022).
14. Liao, C.-T., Wang, Y.-C., Tien, Y.-C., Huang, S.-Y. & Qu, D. Separation of inverse altermagnetic spin-splitting effect from inverse spin hall effect in Ruo 2. *Phys. Rev. Lett.* **133**, 056701 (2024).
15. Liu, Y. et al. Inverse altermagnetic spin splitting effect-induced terahertz emission in Ruo2. *Adv. Opt. Mater.* **11**, 2300177 (2023).
16. Bai, H. et al. Efficient spin-to-charge conversion via altermagnetic spin splitting effect in antiferromagnet Ruo2. *Phys. Rev. Lett.* **130**, 216701 (2023).
17. Fedchenko, O. et al. Observation of time-reversal symmetry breaking in the band structure of altermagnetic Ruo2. *Sci. Adv.* **10**, eadj4883 (2024).
18. Hiraishi, M. et al. Nonmagnetic ground state in Ruo2 revealed by muon spin rotation. *Phys. Rev. Lett.* **132**, 166702 (2024).
19. Keßler, P. et al. Absence of magnetic order in Ruo2: insights from μ sr spectroscopy and neutron diffraction. *npj Spintron.* **2**, 50 (2024).
20. Liu, J. et al. Absence of altermagnetic spin splitting character in rutile oxide Ruo2. *Phys. Rev. Lett.* **133**, 176401 (2024).
21. Seifert, T. et al. Efficient metallic spintronic emitters of ultrabroadband terahertz radiation. *Nat. photonics* **10**, 483–488 (2016).
22. Rouzegar, R. et al. Laser-induced terahertz spin transport in magnetic nanostructures arises from the same force as ultrafast demagnetization. *Phys. Rev. B* **106**, 144427 (2022).
23. Varela-Manjarres, J., Kefayati, A., Jungfleisch, M. B., Xiao, J. Q. & Nikolić, B. K. Charge and spin current pumping by ultrafast demagnetization dynamics. *Phys. Rev. B* **110**, L060410 (2024).
24. Wu, W., Yaw Ameyaw, C., Doty, M. F. & Jungfleisch, M. B. Principles of spintronic thz emitters. *J. Appl. Phys.* **130**, 091101 (2021).
25. Zhang, S. et al. Nonrelativistic and nonmagnetic terahertz-wave generation via ultrafast current control in anisotropic conductive heterostructures. *Adv. Photonics* **5**, 056006–056006 (2023).
26. Momma, K. & Izumi, F. Vesta 3 for three-dimensional visualization of crystal, volumetric and morphology data. *Appl. Crystallogr.* **44**, 1272–1276 (2011).
27. Wu, W. et al. Hybrid terahertz emitter for pulse shaping and chirality control (advanced optical materials 8/2025). *Adv. Opt. Mater.* **13**, 2570069 (2025).
28. Sato, M. et al. Terahertz polarization pulse shaping with arbitrary field control. *Nat. Photonics* **7**, 724–731 (2013).
29. Herrmann, E. et al. Modulators for mid-infrared and terahertz light. *J. Appl. Phys.* **128**, 140903 (2020).
30. Kan, T. et al. Enantiomeric switching of chiral metamaterial for terahertz polarization modulation employing vertically deformable mems spirals. *Nat. Commun.* **6**, 8422 (2015).

Acknowledgements

This research was sponsored by NSF DMR-1904076, NSF through the University of Delaware Materials Research Science and Engineering Center (MRSEC), DMR-2011824, and King Abdullah University of Science and Technology (KAUST), ORFS-2022-CRG11-5031.2.

Author contributions

D.T.P. and J.Q.X. conceived the project. D.T.P. and N.J.P. deposited the films and characterized them by HRXRD and VSM, and also field-annealed the samples. S.B. and X.W. deposited samples that were used for preliminary TDTS measurements (by W.W.) that resolved the substrate birefringence issue via backside incidence excitation. L.S., S.S., and W.W. performed the TDTS measurements with supervision by L.G. and M.B.J. Data analysis was done by D.T.P. with assistance from L.S. and N.J.P. All authors discussed the results and provided feedback.

Competing interests

D.T.P., L.S., S.S., X.W., W.W., L.G., M.B.J., and J.Q.X. are listed as inventors on a pending patent application by the University of Delaware related to observations in this manuscript. The remaining authors declare no competing interest.

Additional information

Supplementary information The online version contains supplementary material available at https://doi.org/10.1038/s44306-025-00083-2.

Correspondence and requests for materials should be addressed to David T. Plouff, Lars Gundlach, M. Benjamin Jungfleisch or John Q. Xiao.